MNRAS 000, 1–9 (2019) Preprint 10 October 2019 Compiled using MNRAS LATEX style file v3.0

MUSEQuBES: Calibrating the redshifts of Lyman-α emitters using stacked circumgalactic medium absorption profiles

Sowgat Muzahid[1,2⋆], Joop Schaye[2], Raffaella Anna Marino[3], Sebastiano Cantalupo[3], Jarle Brinchmann[2,4], Thierry Contini[5], Martin Wendt[1,6], Lutz Wisotzki[1], Johannes Zabl[7], Nicolas Bouché[7], Mohammad Akhlaghi[8,9], Hsiao-Wen Chen[10], Adélaïde Claeyssens[7], Sean Johnson[11,12†], Floriane Leclercq[7,13], Michael Maseda[2], Jorryt Matthee[3], Johan Richard[7], Tanya Urrutia[1], and Anne Verhamme[13]

[1] *Leibniz-Institut für Astrophysik Potsdam (AIP), An der Sternwarte 16, D-14482 Potsdam, Germany*
[2] *Leiden Observatory, Leiden University, PO Box 9513, NL-2300 RA Leiden, the Netherlands*
[3] *Department of Physics, ETH Zürich, Wolfgang-Pauli-Strasse 27, 8093 Zürich, Switzerland*
[4] *Instituto de Astrofísica e Ciências do Espaço, Universidade do Porto, CAUP, Rua das Estrelas, PT4150-762 Porto, Portugal*
[5] *Institut de Recherche en Astrophysique et Planétologie (IRAP), Université de Toulouse, CNRS, UPS, F-31400 Toulouse, France*
[6] *Institut für Physik und Astronomie, Universität Potsdam, Karl-Liebknecht-Str 24/25, D-14476 Golm, Germany*
[7] *Univ Lyon, Univ Lyon1, Ens de Lyon, CNRS, Centre de Recherche Astrophysique de Lyon UMR5574, F-69230, Saint-Genis-Laval, France*
[8] *Instituto de Astrofísica de Canarias, C/ Vía Láctea, 38200 La Laguna, Tenerife, Spain*
[9] *Facultad de Física, Universidad de La Laguna, Avda. Astrofísico Fco. Sánchez s/n, 38200 La Laguna, Tenerife, Spain*
[10] *Department of Astronomy & Astrophysics, The University of Chicago, Chicago, IL 60637, USA*
[11] *Department of Astrophysical Science, 4 Ivy Lane, Princeton University, Princeton, NJ 08644, USA*
[12] *The Observatories of the Carnegie Institution for Science, 813 Santa Barbara Street, Pasadena, CA 91101, USA*
[13] *Observatoire de Genéve, Université de Genéve, 51 Ch. des Maillettes, CH-1290 Versoix, Switzerland*

Accepted. Received; in original form

ABSTRACT

Lyman−α (Lyα) emission lines are typically found to be redshifted with respect to the systemic redshifts of galaxies, likely due to resonant scattering of Lyα photons. Here we measure the average velocity offset for a sample of 96 $z \approx 3.3$ Lyα emitters (LAEs) with a median Lyα flux (luminosity) of $\approx 10^{-17}$ erg cm^{-2} s^{-1} ($\approx 10^{42}$ erg s^{-1}) and a median unobscured star formation rate (SFR) of ≈ 1.3 M$_\odot$ yr^{-1}, detected by the Multi-Unit Spectroscopic Explorer as part of our MUSEQuBES circumgalactic medium (CGM) survey. By postulating that the stacked CGM absorption profiles of these LAEs, probed by 8 background quasars, must be centered on the systemic redshift, we measure an average velocity offset, $V_{\rm offset} = 169 \pm 10$ km s^{-1}, between the Lyα emission peak and the systemic redshift. The observed $V_{\rm offset}$ is lower by factors of ≈ 1.4 and ≈ 2.6 compared to the velocity offsets measured for narrow-band selected LAEs and Lyman break galaxies, respectively, which probe galaxies with higher masses and SFRs. Consistent with earlier studies based on direct measurements for individual objects, we find that the $V_{\rm offset}$ is correlated with the full width at half-maximum of the red peak of the Lyα line, and anti-correlated with the rest-frame equivalent width. Moreover, we find that $V_{\rm offset}$ is correlated with SFR with a sub-linear scaling relation, $V_{\rm offset} \propto {\rm SFR}^{0.16\pm0.03}$. Adopting the mass scaling for main sequence galaxies, such a relation suggests that $V_{\rm offset}$ scales with the circular velocity of the dark matter halos hosting the LAEs.

Key words: galaxies: haloes – galaxies: high-redshift – quasar: absorption lines

1 INTRODUCTION

Lyman-α (Lyα) emitters (LAEs) are galaxies that are identified through the Lyα line of neutral hydrogen (λ1215.67 Å). Owing to the high cosmic abundance of hydrogen and the large oscilla-

⋆ E-mail: sowgat@strw.leidenuniv.nl
† Carnegie–Princeton fellow

tor strength of the $2p \longrightarrow 1s$ transition, Lyα emission has been recognized as an excellent tool to identify galaxies using a variety of techniques, including narrow-band (NB) and medium-band surveys (e.g., Malhotra & Rhoads 2002; Gronwall et al. 2007; Sobral et al. 2018; Shibuya et al. 2018), integral-field-spectroscopy (IFS) surveys (e.g., Wisotzki et al. 2016; Inami et al. 2017; Leclercq et al. 2017; Urrutia et al. 2019), multi-object spectroscopy (e.g., Cassata et al. 2011), and long-slit spectroscopy (e.g., Rauch et al. 2008, 2016). LAEs detected via different techniques can probe a diverse galaxy population, however, there is a growing consensus that the majority of LAEs are typically low-mass, star-forming galaxies (e.g., Gawiser et al. 2007; Hagen et al. 2016; Hao et al. 2018).

Though Lyα is an excellent tool to detect galaxies, particularly at high redshift ($z > 2$), interpreting Lyα emission spectra is challenging because of resonant scattering and susceptibility to dust extinction (e.g., Hayes 2015). The Lyα spectrum emerging from a uniform spherical, static gas cloud with a central Lyα emitting source appears as symmetric double peaked emission with a peak separation that increases with increasing line-center optical depth (e.g., Neufeld 1990; Zheng & Miralda-Escudé 2002; Cantalupo et al. 2005; Verhamme et al. 2006; Dijkstra et al. 2006). Any bulk motion of the gas with respect to the central source, however, makes the peaks asymmetric. For example, outflowing (infalling) gas would enhance the red[1] (blue) peak and suppress the blue (red) peak (e.g., Laursen et al. 2009). In fact, the signature of outflowing gas (i.e., a dominant asymmetric red peak and an occasional weaker blue "bump") is ubiquitous in the spectra of high-z LAEs (e.g., Gronke 2017). Composite spectra of high-z LAEs indeed show signatures of metal enriched outflows with outflow velocity increasing with continuum luminosity (Trainor et al. 2015). Owing to resonant scattering, the Lyα emission line does not trace the systemic redshift. In fact, observations have shown that Lyα redshifts are, on average, shifted by $\approx +230$ km s^{-1} (for LAEs; e.g., Shibuya et al. 2014) to $\approx +440$ km s^{-1}(for Lyman break galaxies (LBGs); e.g., Steidel et al. 2010). The Lyα redshifts should, thus, be taken with caution in the absence of non-resonant rest-frame ultraviolet (UV)/optical stellar absorption and/or nebular emission lines which provide the most accurate galaxy redshifts.

Recently, Verhamme et al. (2018) suggested two empirical relations to recover the systemic redshift of galaxies from their Lyα line profile using the observed correlations between (i) the velocity offset (measured from non-resonant UV/optical lines) and the full width at half-maximum (FWHM) of the red peak of the Lyα line; (ii) the velocity offset and the velocity separation between the red peak and the blue bump. Erb et al. (2014) reported $> 3\sigma$ correlations between velocity offset and $R-$band magnitude, M_{UV}, and the velocity dispersion of nebular emission lines for a sample of 36 LAEs at $z \approx 2-3$. In addition, a strong anti-correlation ($> 7\sigma$) was found between velocity offset and the Lyα equivalent width (EW_0). Such empirical relationships are valuable for understanding the physics of the Lyα emitting galaxies, and provide indirect means to obtain the systemic redshifts. Finding and confirming such empirical relations and observational trends using complementary techniques is thus important.

Obtaining accurate systemic redshifts is particularly important for studying the circumgalactic medium (CGM) of galaxies using background quasars, since the association of galaxies with their CGM absorption lines, seen in the quasar spectrum, is based on velocity coincidence. CGM studies in the literature typically adopt a velocity window of ± 500 km s^{-1} around the galaxy redshift to search for associated CGM absorption. It is thus essential to know the galaxy redshifts with an accuracy of $\Delta z/(1+z) \approx 10^{-3}$ or better. Using guaranteed time observations with the Multi-Unit Spectroscopic Explorer (MUSE; Bacon et al. 2010), we conducted the MUSEQuBES (MUSE Quasar-field Blind Emitters Survey) survey– a blind search for LAEs in $1' \times 1'$ fields centered on 8 bright $z \approx 3.6-3.8$ quasars (see Table 1). This is the first systematic survey of the CGM of LAEs in absorption (Muzahid et al., in preparation). Since, we generally do not have access to stellar absorption and/or non-resonant nebular emission lines for the LAEs in our sample, we must make use of the Lyα redshifts ($z_{\rm peak}$; determined from the peak of the Lyα line). Here we adopt the approach proposed by Rakic et al. (2011) to calibrate the Lyα redshifts in a statistical manner using mean/median stacked CGM absorption (H I Lyα) profiles, by requiring that the average CGM absorption profiles must be centered on the systemic velocity since the LAEs are randomly oriented with respect to the background quasar. Rakic et al. (2011) applied this technique to a large sample of $z \approx 2.3$ LBGs, finding velocity offsets that agreed with the direct measurements from non-resonant nebular lines available for a subset of their sample.

Table 1. The data sample

Quasar Field (1)	RA_{QSO} (2)	Dec_{QSO} (3)	z_{QSO} (4)	t_{exp} (5)	N_{LAE} (6)
Q1422+23	14:24:38.1	+22:56:01	3.620	4	8
Q0055−269	00:57:58.1	−26:43:14	3.655	10	12
Q1317−0507	13:20:30.0	−05:23:35	3.700	10	22
Q1621−0042	16:21:16.9	−00:42:50	3.709	9	12
QB2000−330	20:03:24.0	−32:51:44	3.773	10	14
PKS1937−101	19:39:57.3	−10:02:41	3.787	3	2
J0124+0044	01:24:03.0	+00:44:32	3.834	2	4
BRI1108−07	11:11:13.6	−08:04:02	3.922	2	22

Notes– (1) Name of the quasar field; (2) Right Ascension (J2000), (3) Declination (J2000), and (4) Redshift of the quasar; (5) MUSE exposure time of the field in hour; (6) Number of detected LAEs in the redshift range of interest.

This paper is organized as follows: In Section 2 we briefly describe the observations and data reduction procedures. In Section 3 we summarize the properties of our LAE sample. Section 4 presents the main results, followed by a discussion in Section 5. Section 6 concludes the paper. Throughout this study, we adopt a flat ΛCDM cosmology with $H_0 = 70$ km s^{-1} Mpc^{-1}, $\Omega_{\rm M} = 0.3$ and $\Omega_\Lambda = 0.7$. All distances given are in physical units.

2 OBSERVATIONS & DATA REDUCTION

Our MUSEQuBES survey utilizes $\approx$ 50h of MUSE GTO observations in the wide field mode centered on 8 high-z quasars that have high quality (S/N > 50 per pixel) optical spectra obtained with the Very Large Telescope Ultraviolet and Visual Echelle Spectrograph (VLT/UVES) and/or Keck HIgh Resolution Echelle Spectrometer (Keck/HIRES). The details of the quasar fields are given in Table 1. The MUSE and UVES/HIRES observations and data reduction procedures will be presented in Muzahid et al., (in preparation). The MUSE data for four of the eight quasar fields (Q0055−269, Q1317−0507, Q1621−0042, and Q2000−330) were reduced using the standard MUSE pipeline `v1.6` (Weilbacher et al. 2012) and post-processed with the tools in the CubExtractor package (`CubEx v1.6`; Cantalupo in preparation; see Cantalupo et al. 2019, for a description) to improve flat-fielding and sky subtraction as presented

[1] The lower energy (higher wavelength) peak.

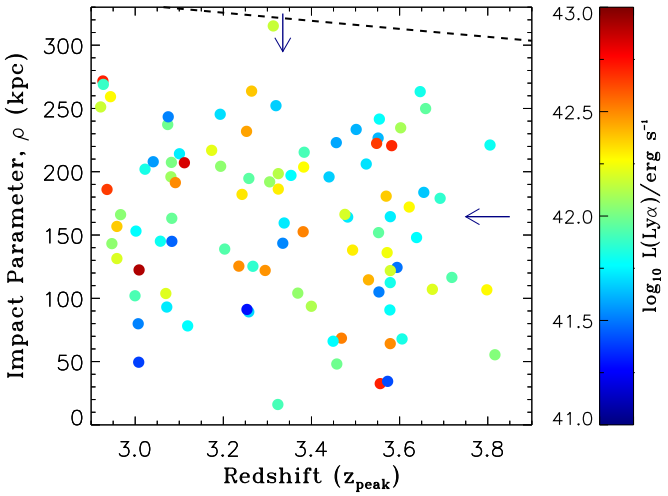

Figure 1. Scatter plot of impact parameter versus redshift of the 96 LAEs. The data points are color coded by the Lyα luminosity. The median impact parameter and median redshift are indicated by the arrows. The maximum impact parameter allowed by the MUSE FoV is shown by the dashed line on the top.

in Marino et al. (2018). The remaining fields were reduced using the MUSE pipeline software (`v2.4`) and post-processed with `CubEx v1.6` following the same procedures.

The optical spectra of the quasars were obtained primarily using VLT/UVES with resolution, $R \approx 45000$. The final coadded and continuum normalized spectra were downloaded from the SQUAD database (Murphy et al. 2019) for all but Q1422+23. The spectrum of the quasar Q1422+23 was reduced using the Common Pipeline Language (`CPL v6.3`) of the UVES pipeline. After the standard reduction, the custom software UVES Popler[2] was used to combine the extracted echelle orders into single 1D spectra. The coadded spectrum was continuum normalized by low-order spline interpolation to the absorption line free regions determined by iterative sigma-clipping. Keck/HIRES data are available for four quasars: BRI1108–07, PKS1937–101, QB2000–330, and Q1422+23. We used the HIRES spectra of PKS1937–101 and Q1422+23 from the KODIAQ data release (O'Meara et al. 2015) to fill in the gaps in the UVES spectra. We combined the continuum normalized UVES and HIRES spectra using inverse-variance weighting. Air-to-vacuum conversion was done for both the MUSE and UVES spectra before performing any measurements.

For the CGM spectral stacking analysis we have first used the pixel optical depth method (Cowie & Songaila 1998; Aguirre et al. 2002; Schaye et al. 2003; Turner et al. 2014) using the python module `PODPy` developed by Turner et al. (2014). `PODPy` iteratively examines whether the optical depth of a given pixel in a quasar spectrum is consistent with being the transition of interest (e.g., Lyα, C IV). `PODPy` corrects for contamination by flagging the pixels whose optical depths are not consistent with the expectation. For multiplets, it uses all available transitions (up to Lyη for H I) leading to a larger dynamic range in the "recovered" optical depth. We refer the reader to Appendix A of Turner et al. (2014) for more details. The optical depth recovered by `PODPy` was then converted to flux before stacking the quasar spectra.

3 THE LAE SAMPLE

We used `CubEx v1.6` (Cantalupo et al. 2019) for automatic extraction of emission line sources in the MUSE datacubes. `CubEx` uses a 3D extension of the connected-component labeling algorithm. The source extraction and classification procedure will be presented in detail in Muzahid et al., (in preparation). Briefly, after spatially smoothing (by 2 pixels radius) the datacubes and the corresponding variances at each wavelength layer, we require three conditions to be satisfied for a detection: (i) S/N per voxel > 4.0, (ii) number of connected voxels $N_{\rm vox} > 40$, and (iii) a spectral S/N > 4.5 measured on the 1D Lyα emission line spectrum. All the extracted objects are then visually inspected (both 1D spectra, extracted using the segmentation maps produced by `CubEx`, and pseudo-NB images around the emission features) and classified by two members of the team (SM and RAM) independently.

A total of 96 LAEs have been detected in the 8 MUSE cubes. The impact parameters (ρ) of the LAEs from the quasar sight lines are plotted against the Lyα peak redshifts ($z_{\rm peak}$) in Fig. 1. The redshifts of the LAEs are determined directly from the peak of the emission lines in the 1D spectra without any modelling. We ensured that $z_{\rm peak}$ is not affected by noise-spikes by visually inspecting the spectra. In case of double peaked emission we used the red peak for the $z_{\rm peak}$ measurement. The minimum $z_{\rm peak}$ ($\approx$2.9) is determined by the lowest wavelength covered by MUSE. Note that we did not use the first 8–10 wavelength layers ($\approx$ 10 Å) in our search, in order to avoid a large number of spurious detections at the very edge of the spectrum. The maximum $z_{\rm peak}$ is determined by the quasar redshift ($z_{\rm QSO}$). In order to exclude the quasars' proximity regions (see e.g., Muzahid et al. 2013), we did not use the 3000 km s^{-1} bluewards of the $z_{\rm QSO}$. The LAEs in our sample span a redshift range of 2.92–3.82 with a median $z_{\rm peak}$ of 3.33. The maximum and minimum ρ values are determined by the MUSE field-of-view and the quasars' point spread functions (PSFs), respectively. The ρ values span 16–315 kpc with a median of 165 kpc.

The data points in Fig.1 are color coded by the Lyα luminosity, L(Lyα), calculated from the Galactic extinction corrected line flux, f(Lyα)[3]. The f(Lyα) values are measured from pseudo-NB images using the curve-of-growth method following Marino et al. (2018). The f(Lyα) values are found to be in the range $10^{-17.7}$ – $10^{-16.0}$ erg cm^{-2} s^{-1} with a median value of $10^{-17.0}$ erg cm^{-2} s^{-1}. The L(Lyα) spans $10^{41.3}$ – $10^{42.9}$ erg s^{-1} with a median value of $10^{42.0}$ erg s^{-1}. Following Verhamme et al. (2018), the FWHM (of the red peak for the handful of double peaked profiles) is calculated directly from the 1D spectrum, without any modelling and without correcting for instrumental broadening, as the velocity width of the Lyα emission line with flux above half of the maximum flux value. The FWHM values span the range 120–528 km s^{-1} with a median value of 240 km s^{-1}. Here we note that 10 LAEs show FWHM lower than the MUSE spectral resolution of $\approx$ 166 km s^{-1} at the median Lyα wavelength of our sample.

The UV continuum fluxes, $f_{\rm UV}$, and the associated errors are derived by integrating the 1D spectra, extracted from the original cubes (not continuum subtracted) and the corresponding variance cubes using the same segmentation maps used to obtain the 1D Lyα emission spectra. We chose a wavelength range of rest-frame 1410–1640 Å, the same as the wavelength range covering the FWHM of the *GALEX* far-UV transmission curve. No $f_{\rm UV}$ are calculated for

[2] https://doi.org/10.5281/zenodo.44765

[3] We used the E(B − V) values from Schlafly & Finkbeiner (2011) and the Fitzpatrick (1999) extinction curve to de-redden the fluxes.

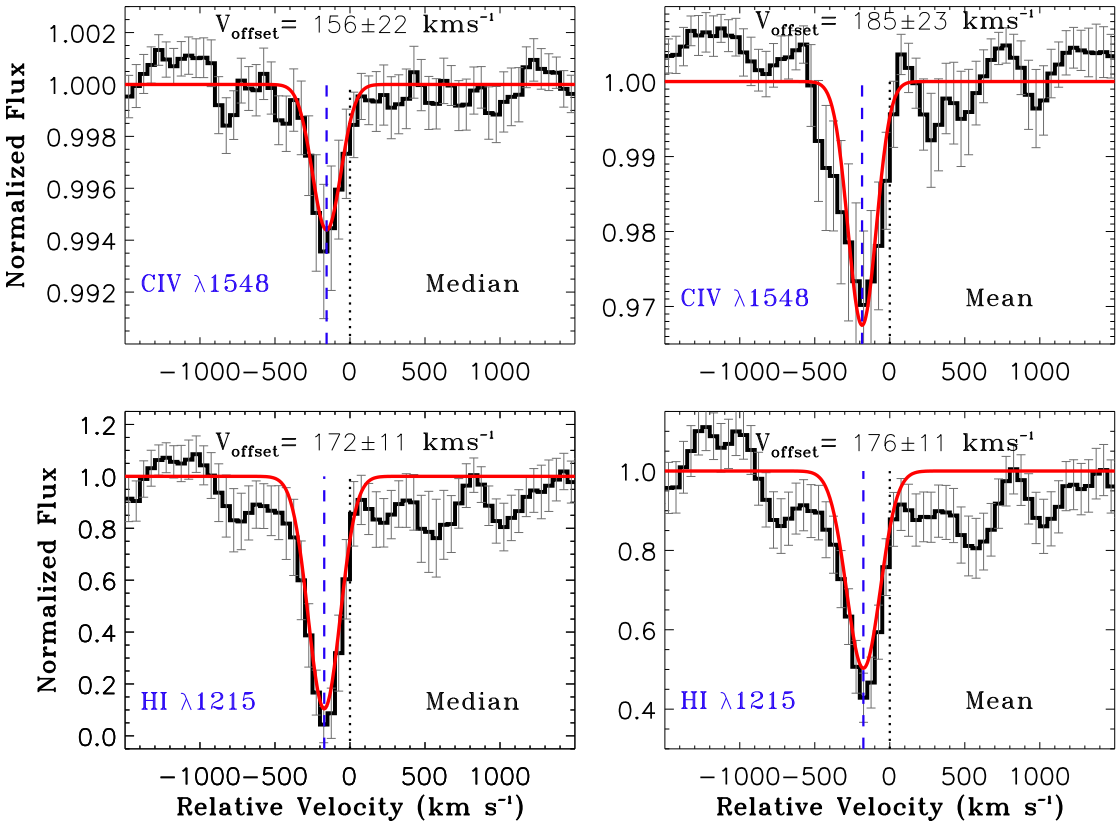

Figure 2. Median (left) and mean (right) stacked CGM absorption profiles of H I λ1215 (bottom) and C IV λ1548 (top). The zero velocity ($V_{\rm peak}$) is defined by $z_{\rm peak}$, the redshift of peak Lyα emission. The profiles are normalized to the pseudo-continuum estimated far away from zero velocity. The 1σ errors are calculated from 1000 bootstrap realizations of the LAE sample. The best-fitting Gaussian profiles are shown by the smooth red curves. The centroids of the Gaussians ($V_{\rm CGM}$), marked by the blue vertical dashed lines, provide the velocity offset, $V_{\rm offset} \equiv (V_{\rm peak} - V_{\rm CGM})$. $V_{\rm offset}$ measured for the different stacked profiles are indicated in the corresponding panels. The weighted average of the $V_{\rm offset}$ values is 169 ± 10 km s^{-1} (178 ± 10 km s^{-1}) for the median (mean) stacked profiles.

the 15 LAEs that are contaminated by low-z continuum sources. About 48% (39/81) of the remaining LAEs are detected in UV continuum emission with > 5σ significance. For the 39 continuum detected objects, $f_{\rm UV}$ values (corrected for Galactic extinction) are in the range $10^{-17.0}$ – $10^{-15.6}$ erg cm^{-2} s^{-1} with a median of $10^{-16.4}$ erg cm^{-2} s^{-1}. For the remaining 42 LAEs for which we could place meaningful 5σ upper limits, the $f_{\rm UV}$ values were found to be lower than $10^{-16.4}$ erg cm^{-2} s^{-1}. The UV continuum luminosity, $L_{\rm UV}$, ranges from $10^{42.1}$ – $10^{43.4}$ erg s^{-1} for the continuum detected objects (median $10^{42.7}$ erg s^{-1}). For the non-detections, the upper limits on $L_{\rm UV}$ are in the range of $10^{41.9}$ – $10^{42.7}$ erg s^{-1}.

The dust-uncorrected SFRs are calculated from the measured $L_{\rm UV}$ values using the local calibration relation of Kennicutt (1998) corrected to the Chabrier (2003) initial mass function (IMF; see Madau & Dickinson 2014). The SFRs for the continuum detected LAEs span 0.3 – 7.1 M$_\odot$ yr^{-1} with a median SFR of 1.3 M$_\odot$ yr^{-1}. For the continuum un-detected LAEs, the SFRs are < 1.5 M$_\odot$ yr^{-1}. The rest-frame equivalent width of the Lyα emission (EW$_0$) is obtained by dividing the Lyα line flux by the continuum flux density and then divided by (1 + $z_{\rm peak}$). The continuum flux density is estimated from the extrapolation of the measured continuum at rest-frame 1500 Å assuming a UV continuum slope ($\beta_{\rm UV}$) of −2.0 (Bouwens et al. 2014). The continuum detected objects have EW$_0$ in the range 9–113 Å with a median EW$_0$ of 48 Å.

In our redshift range of interest ($z \approx$ 3–4), the presence of the non-resonant C III] $\lambda\lambda$1907,1909 doublet in the MUSE spectra is an excellent means to obtain the systemic redshift. We detect the C III] $\lambda\lambda$1907,1909 doublet for only 3 LAEs, one of them being tentative. Such a low detection rate of the C III] line is consistent with the recent results of Maseda et al. (2017).

4 RESULTS

The median and mean stacked absorption profiles of H I Lyα and C IV, arising from the CGM of the LAEs, are shown in Fig. 2. For each transition (H I λ1215 or C IV λ1548), we have selected the part of the quasar spectrum covering a velocity range of −3000 to +3000 km s^{-1} with respect to the $z_{\rm peak}$ for a given LAE. The mean and median fluxes for the full sample are then calculated from the PODPy "recovered" pixel optical depths in bins of 50 km s^{-1}. We note here that our main conclusions remain valid even if we use the original quasar spectra for stacking instead of using PODPy recovered spectra. However, in that case the stacked profiles become noisier, particularly when we split the sample into different sub-samples. We thus chose to use the PODPy recovered spectra.

Fig. 2 shows the first measurements of the CGM of LAEs in absorption for a statistically meaningful sample (see Díaz et al. 2015 and Zahedy et al. 2019, for individual examples). We detect absorption signals for H I and C IV with > 5σ significances.

Table 2. Velocity offset measurements for different sub-samples

Sub-sample	Threshold	Median	16^{th} percentile	84^{th} percentile	N_{LAE}	V_{offset} (H I) (Median)	V_{offset} (H I) (Mean)	V_{offset} (C IV) (Median)	V_{offset} (C IV) (Mean)	V_{offset} (H I+C IV) (Median)	V_{offset} (H I+C IV) (Mean)
(1)	(2)	(3)	(4)	(5)	(6)	(7)	(8)	(9)	(10)	(11)	(12)
Low–ρ	164.5	114.6	66.1	148.0	48	177 ± 11	172±13	163±24	194±13	175±10	183 ± 9
High–ρ	164.5	214.2	183.7	251.2	48	160 ± 16	158±16	169±25	163±35	162±10	159 ± 15
Low–z_{peak}	3.335	3.083	2.959	3.2671	48	204 ± 18	197±17	166±24	166±28	190±14	189 ± 15
High–z_{peak}	3.335	3.556	3.400	3.6548	48	155 ± 6	159±11	146±37	209±20	155 ± 6	171 ± 10
Low–FWHM	239.7	195.0	161.6	227.2	48	151 ± 14	161±16	155±29	160±21	152±13	161 ± 13
High–FWHM	239.7	289.2	255.5	356.6	48	189 ± 12	183±13	167±36	202±38	187±11	185 ± 12
Low–$FWHM^{a}_{resolved}$	253.1	214.2	184.2	237.3	43	145 ± 15	153±16	134±22	149±22	142±12	152 ± 13
High–$FWHM^{a}_{resolved}$	253.1	290.5	258.4	376.2	43	194 ± 16	190±16	178±46	200±43	192±15	191 ± 15
Low–$FWHM^{b}_{matched-z_{peak}}$	239.7	201.9	164.3	228.0	31	140 ± 16	147±18	131±32	155±28	138±14	149 ± 15
High–$FWHM^{b}_{matched-z_{peak}}$	239.7	290.5	252.4	387.0	31	204 ± 13	205±15	168±45	230±43	201±13	208 ± 14
Low–$z^{c}_{matched-FWHM}$	3.335	3.083	3.000	3.305	37	187 ± 16	185±14	185±36	177±26	187±15	183 ± 12
High–$z^{c}_{matched-FWHM}$	3.335	3.570	3.400	3.660	37	156 ± 6	164±10	153±64	207±28	156 ± 6	169 ± 9
Low–log L(Lyα)	41.97	41.76	41.52	41.91	48	163 ± 13	160±14	141±37	214±19	161±12	179 ± 11
High–log L(Lyα)	41.97	42.28	42.05	42.52	48	184 ± 13	183±13	171±28	154±26	182±12	177 ± 12
Low–log SFR^{d}	−0.18	−0.38	−0.50	−0.26	33	158 ± 11	163±12	140±27	140±17	155±10	155 ± 10
High–log SFR^{d}	−0.18	0.23	0.01	0.49	30	201 ± 15	192±13	222±43	218±26	203±14	197 ± 12
Low–EW^{d}_{0}	63.3	33.2	19.8	54.1	29	202 ± 10	200±12	231±43	239±21	203±10	210 ± 10
High–EW^{d}_{0}	63.3	94.0	68.8	126.0	30	140 ± 10	146±12	147±19	116±13	141 ± 9	132 ± 9

Notes– (1) The sub-sample for which V_{offset} is measured. (2) The threshold value of the parameter based on which the sub-sample is made: ρ in kpc, FWHM in km s^{-1}, L(Lyα) in erg s^{-1}, SFR in $M_\odot$ yr^{-1}, and EW_0 in Å. (3) The median value of the parameter for the sub-sample. (4) 16^{th} percentile of the parameter. (5) 84^{th} percentile of the parameter. (6) Number of LAEs contributing to the stack. (7) The velocity offset in km s^{-1} measured from the median stacked H I profile. (8) The same as (7) but for the mean stacked H I profile. (9) The same as (7) but for the median stacked C IV profile. (10) The same as (7) but for the mean stacked C IV profile. (11) The weighted average of V_{offset} measured from the median stacked H I and C IV profiles. (12) The same as (11) but measured from the mean stacked H I and C IV profiles.

[a] The LAEs with FWHM smaller than the MUSE resolution (< 166 km s^{-1}) are excluded.

[b] The z_{peak} is matched for these two sub-samples.

[c] The FWHM is matched for these two sub-samples.

[d] The LAEs that are blended with low-z continuum objects are excluded. Upper/lower limits are considered as detections in the median and percentile calculations.

Note that, none of the stacked absorption profiles are centered on the 0 km s^{-1} defined by the redshift of peak Lyα emission, z_{peak}. All profiles show velocity offset, V_{offset} > 150 km s^{-1}. Here $V_{offset} = (V_{peak} - V_{CGM})$, where V_{CGM} is the velocity centroid of the CGM absorption profile, and V_{peak} is the velocity corresponding to z_{peak}. The V_{offset} measured for the median (mean) stacked H I profile is 172 ± 11 km s^{-1} (176 ± 11 km s^{-1}). The velocity offsets and the associated errors are determined from Gaussian fits. Moreover, the median and mean stacked C IV profiles show V_{offset} of 156 ± 22 km s^{-1}and 185 ± 23 km s^{-1}, respectively. Owing to the relative weakness of the C IV absorption, the estimated errors on the corresponding V_{offset} measurements are larger. Nevertheless, the stacked C IV profiles provide independent measurements of V_{offset}, and are fully consistent with the H I measurements. The weighted average of the V_{offset} values measured from the median and mean stacked profiles are 169 ± 10 km s^{-1} and 178 ± 10 km s^{-1}, respectively. Such offsets imply that the z_{peak} values are systematically redshifted with respect to the systemic redshifts, consistent with the results from the observations of non-resonant rest-frame UV/optical nebular emission/absorption lines (e.g., Steidel et al. 2010; Shibuya et al. 2014; Verhamme et al. 2018).

In order to investigate possible trends between V_{offset} and other parameters (e.g., z_{peak}, ρ, FWHM), we generated stacked H I and C IV absorption profiles for several sub-samples corresponding to different parameters, as summarized in Table 2. The velocity offsets and corresponding uncertainties, determined from Gaussian fits to the stacked H I and C IV profiles (as in Fig. 2), for the different sub-samples are also listed in the table. The last two columns (columns 11 & 12) provide the combined constraints on V_{offset}, obtained from the inverse variance weighted average of the velocity offsets measured from the H I and C IV profiles, and are illustrated in Fig. 3. We will only use these weighted average V_{offset} values in all further discussions.

It is evident from Fig. 3 that V_{offset} does not show any significant trend with ρ and L(Lyα). The difference in V_{offset} between the corresponding "high" and "low" sub-samples, calculated for both the mean and median stacked profiles, has < 1.5σ significance. There is a 2.3σ (1.0σ) difference between the V_{offset} values measured from the median (mean) stacked profiles of the low– and high–z_{peak} sub-samples. However, we note that the trend is actually driven by FWHM, owing to a 3.4σ anti-correlation between z_{peak}

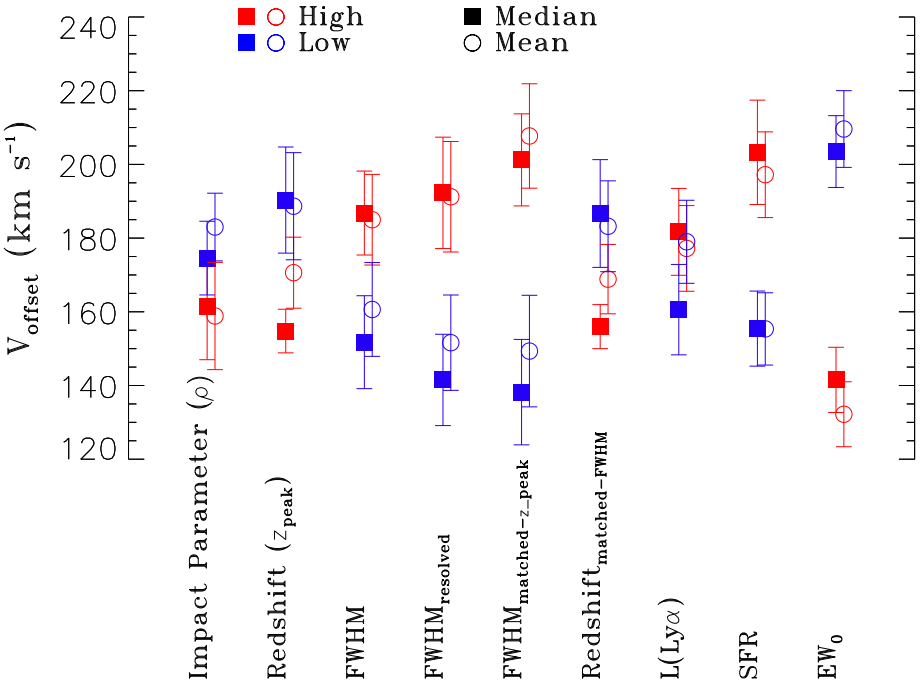

Figure 3. The inverse variance weighted average of the velocity offsets measured from the H I and C IV absorption profiles for the different sub-samples listed in Table 2. The velocity offsets measured from the median and mean stacked profiles are indicated by the filled squares and open circles respectively. The red and blue points correspond to the "high" and "low" sub-samples (Table 2), respectively. V_{offset} shows significant trends with FWHM, SFR, and EW$_0$.

and FWHM (Spearman rank correlation coefficient, $r_s = -0.35$) [4]. Indeed, the difference reduces to $< 2\sigma$ when the low– and high–z_{peak} sub-samples are matched in FWHM.

There is a 2.0σ (1.4σ) difference in the V_{offset} for the high–FWHM and low–FWHM sub-samples measured from the median (mean) stacked profiles. However, the difference increases for the FWHM$_{resolved}$ sub-samples, from which we excluded the LAEs with FWHM smaller than the MUSE resolution, to 2.6σ (2.0σ for the mean stack). Since we noted an anti-correlation between z_{peak} and FWHM, it is important to investigate whether the trend between V_{offset} and FWHM remains when the low– and high–FWHM sub-samples are matched in z_{peak}. In fact, we do find a 2.9σ (3.3σ for the mean stack) difference in V_{offset} between the low– and high–FWHM sub-samples when they are matched in z_{peak}. In addition, a clear difference, with $> 2.5\sigma$ significance, is seen in V_{offset} measured for the low– and high–SFR sub-samples, for both the mean and median stacked profiles. Finally, the strongest difference ($> 4.5\sigma$) in V_{offset} is seen between the low– and high–EW$_0$ sub-samples, with higher EW$_0$ yielding a smaller velocity offset. In the next section we discuss the possible implications of these new results in the context of existing observational and theoretical studies.

5 DISCUSSION

Simple, idealized models of Lyα radiation transfer with a central ionizing point source surrounded by a homogeneous, spherically symmetric shell of gas with a range of neutral hydrogen column density (N(H I)), dust opacity, velocity, and temperature (the so-called "shell model", see e.g., Zheng & Miralda-Escudé 2002; Verhamme et al. 2006) have been surprisingly successful in explaining a large variety of Lyα line profiles (e.g., Hashimoto et al. 2015; Gronke 2017). Using the shell model, Verhamme et al. (2018) found a correlation between FWHM and V_{offset} (see also Claeyssens et al. 2019). The left panel of Fig. 4 shows the weighted average V_{offset}, measured from the median stacked CGM absorption (H I and C IV) profiles, against the median FWHM of the low– and high–FWHM$_{resolved}$ sub-samples (blue squares). Consistent with the model prediction, the stacked CGM absorption profiles show larger velocity offsets for the high–FWHM$_{resolved}$ sub-sample (Table 2). The dashed line shows the empirical relation between V_{offset} and FWHM obtained by Verhamme et al. (2018) from the sample of LAEs with known systemic redshifts as indicated by the star symbols. Verhamme et al. (2018) used the LST_LINEFIT routine of Cappellari et al. (2013), which includes a procedure for the rejection of outliers, and obtained a slope of 0.9 ± 0.14, an intercept of -34 ± 60 km s^{-1}, and an intrinsic scatter of 72 ± 12 km s^{-1}. The slope (0.66) and intercept (2 km s^{-1}) we obtain from the stacked CGM absorption profiles are broadly consistent with Verhamme et al. (2018). Note that the trend between V_{offset} and FWHM found by Verhamme et al. (2018) was determined via observations of the interstellar medium (ISM) properties (nebular emission lines) whereas we confirm the same trend using CGM observations.

Steidel et al. (2010) obtained a mean velocity offset of 445 ± 27 km s^{-1} between Lyα and systemic redshifts defined by the Hα lines for a sample of 41 $z \approx 2.3$ LBGs. The total baryonic masses estimated for those LBGs are $\gtrsim 10^{10} - 10^{11.5}$ M$_\odot$. Using a sample of 22 NB-selected (with a typical bandwidth of $\approx$ 100 Å) LAEs with Lyα equivalent widths > 50 Å, Shibuya et al. (2014) obtained

[4] The anti-correlation between z_{peak} and FWHM is likely due to the fact that the MUSE resolution improves from $\approx$ 180 km s^{-1} to $\approx$ 150 km s^{-1} between $z \approx 3.0$ and 3.6.

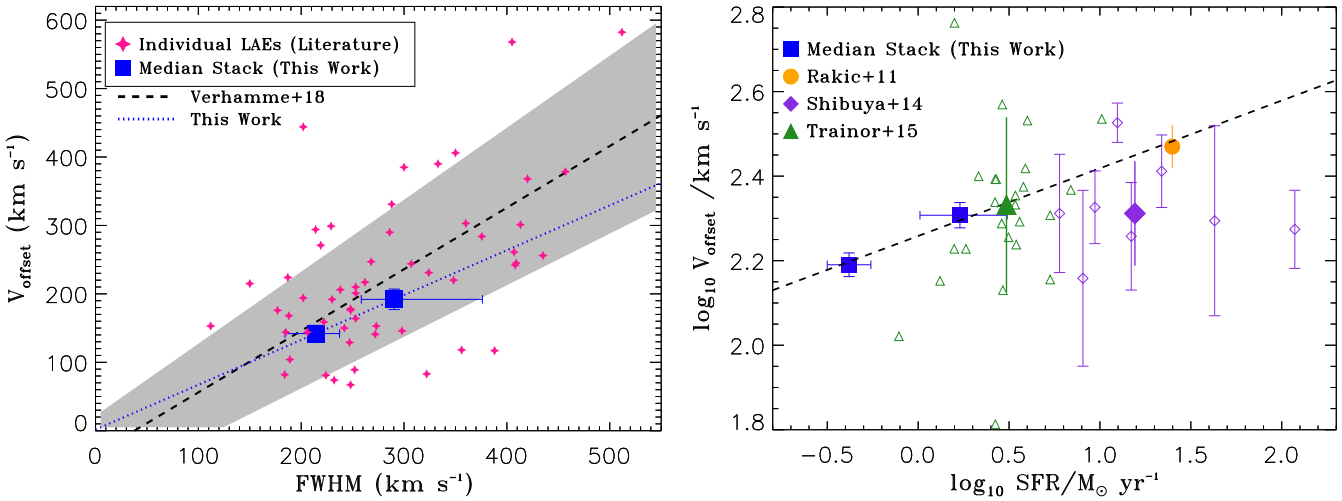

Figure 4. Left: $V_{\rm offset}$ as a function of FWHM of the Lyα line. The star symbols represent LAEs from the literature for which the systemic redshifts are known (see Verhamme et al. (2018) for details). The dashed line and the shaded region represent the best-fit linear relation, $V_{\rm offset}$= 0.9(±0.14)×FWHM − 34(±60) km s^{-1}, for the star symbols and its 1σ range, respectively, as found by Verhamme et al. (2018). The blue squares represent our weighted average $V_{\rm offset}$ measurements for the FWHM$_{\rm resolved}$ sub-samples as in Table 2. The dotted straight line connecting the blue squares has a slope (0.66) and an intercept (2) that are broadly consistent with the empirical relation of Verhamme et al. (2018). Right: Weighted average $V_{\rm offset}$, measured from the median stacked profiles, as a function of SFR for our sample (blue squares). The orange filled circle represents the measurement from Rakic et al. (2011) for $z \approx 2.3$ LBGs. The best-fit linear relation between log $V_{\rm offset}$ and log SFR (log $V_{\rm offset}$ = (0.16 ± 0.03) log SFR + (2.26 ± 0.02)) for those three points is indicated by the dashed line. The open diamonds and the open triangles represent data points from Shibuya et al. (2014) and Trainor et al. (2015), respectively (see text). The filled diamond and the filled triangle represent the median SFR and the median $V_{\rm offset}$ of the corresponding samples, with the error bars indicating the standard deviations. In both panels, the error bars along the x-axis indicate 68 percentile ranges.

an average velocity offset between Lyα and nebular redshifts of 234±9 km s^{-1}. The stellar mass (M_*) estimates for the LAEs in their sample range between $\approx 10^9$ and 10^{10} M$_\odot$. Clearly, the NB-selected LAEs exhibit a smaller velocity offset compared to the broadband–(UV color) selected LBGs (as already noted by Hashimoto et al. 2013, 2015; Shibuya et al. 2014). Hashimoto et al. (2015) argued that the low $V_{\rm offset}$ of LAEs compared to LBGs are related to smaller N(H I) in LAEs. Note that, both LBGs and NB-selected LAEs show higher velocity offsets (by factors of ≈ 2.6 and ≈ 1.4, respectively) compared to what we measure for the MUSE-detected LAEs.

Using the mean H I CGM absorption profile of ≈300 UV color selected galaxies in the redshift range 2 − 3, Rakic et al. (2011) estimated $V_{\rm offset}$ = 295 ± 35 km s^{-1}, which is ≈ 1.7 times higher than what we obtained for our sample. The galaxies in Rakic et al. (2011) were drawn from Steidel et al. (2010) with a typical halo mass of $\sim 10^{12}$ M$_\odot$ (Rakic et al. 2013). Using clustering properties of LAEs, Khostovan et al. (2018) found a strong, redshift-independent correlation between L(Lyα) normalized by the characteristic line luminosity, $L^\star(z)$, and dark matter halo mass. According to their Eq. 13, the median L(Lyα) of our sample of $\approx 10^{42}$ erg s^{-1} (L(Lyα)/$L^\star(z)$ = 0.2)[5] would correspond to a halo mass of $M_h \sim 10^{10.8}$ M$_\odot$, corresponding to a stellar mass of $M_* \sim 10^{8.0}$ M$_\odot$ (Moster et al. 2013), assuming LAEs are average main sequence galaxies. Additionally, the median SFR (1.3 M$_\odot$ yr^{-1}) of our sample corresponds to $M_* \sim 10^{8.6}$M$_\odot$ (Behroozi et al. 2019) and $M_h \sim 10^{11.1}$M$_\odot$ (Moster et al. 2013). Clearly, the MUSE-detected LAEs in our sample are, on average, at least an order of magnitude lower in mass than the LBG sample of Rakic et al. (2011). Higher mass galaxies tend to have higher SFR which, in turn, can drive high velocity, galactic-scale winds causing higher (red) shift of the Lyα emission line.

We find a positive (negative) trend between $V_{\rm offset}$ and SFR (EW$_0$), consistent with the findings of Erb et al. (2014). The anti-correlation between $V_{\rm offset}$ and EW$_0$ is understood in terms of higher optical depth of gas with near systemic velocity (Steidel et al. 2010; Erb et al. 2014). The right panel of Fig. 4 shows the $V_{\rm offset}$ measured from the median stacked profiles against the median SFRs of the low– and high–SFR sub-samples. In addition, we show the $V_{\rm offset}$ measurement from Rakic et al. (2011) for their sample of $z \approx 2.3$ LBGs with a median SFR of ≈ 25 M$_\odot$ yr^{-1} (Turner et al. 2014; Steidel et al. 2014). A positive trend between $V_{\rm offset}$ and SFR is evident in the log − log plot. A linear least-squares fit to the data points results in a slope of 0.16 ± 0.03 and an intercept of 2.26 ± 0.02, indicating a sub-linear relationship $V_{\rm offset} \propto {\rm SFR}^{0.16\pm0.03}$. The relation holds over almost 2 orders of magnitude range in SFR.

Note that the SFRs in our sample are not corrected for dust, whereas the SFRs for the LBG sample of Rakic et al. (2011) are dust-corrected. Using the mean $\beta_{\rm UV}$ of −2.03 estimated for $\sim 0.1L^\star$ galaxies at $z \approx 4$ by Bouwens et al. (2014) and the relationship between $\beta_{\rm UV}$ and UV extinction (A_{1600}) from Meurer et al. (1999)[6], we obtain a mild ≈ 0.15 dex correction in SFR for our sample. Incorporating such a correction factor in SFR provides a consistent best-fitting relationship between $V_{\rm offset}$ and SFR (i.e., a slope of 0.17 ± 0.04 and an intercept of 2.23 ± 0.02).

The open diamonds and the open triangles in the right panel of Fig. 4 represent individual LAEs from Shibuya et al. (2014) and Trainor et al. (2015), respectively, for which the SFRs and $V_{\rm offset}$ values, measured from non-resonant nebular lines, are known. The SFRs for the Trainor et al. (2015) sample are calculated from the

[5] $\log L^\star(z = 3.3)/{\rm erg\ s^{-1}} = 42.68^{+0.07}_{-0.06}$, see Table 2 of Khostovan et al. (2018)

[6] $A_{1600} = 4.43 + 1.99 \times \beta_{\rm UV}$

Hα luminosities using Kennicutt (1998) relation. The SFRs of all these LAEs have been corrected to the Chabrier (2003) IMF. The median SFRs and the median $V_{\rm offset}$ values of these samples are indicated by the corresponding filled symbols. If we include these two points in the fit, we obtain a slope of 0.15 ± 0.03 and an intercept of 2.26 ± 0.02, which are fully consistent with what we obtained earlier.

The correlation between SFR and $V_{\rm offset}$ can be explained as follows. Galaxies with higher SFRs are likely to drive higher velocity winds. Higher velocity winds will enhance and shift the red Lyα peak to a longer wavelength resulting in a larger velocity offset (see Fig. 8 of Laursen et al. 2009, for example). Using the scaling relations between SFR and M_* (SFR $\propto M_*$ at $z \approx 4$; see e.g., Fig. 3 of Behroozi et al. 2019), and between M_* and M_h ($M_* \propto M_h^2$ at $z \approx 4$; e.g., Moster et al. 2013), we obtain $V_{\rm offset} \propto V_{\rm cir}$, where $V_{\rm cir}$ ($\propto M_h^{1/3} \propto M_*^{1/6} \propto {\rm SFR}^{1/6}$) is the halo circular velocity. It is interesting to note that in models of momentum driven galactic outflows the wind speed scales as $V_{\rm cir}$ (e.g., Murray et al. 2005; Heckman et al. 2015). Moreover, models of Lyα radiative transfer suggest that $V_{\rm offset}$ is twice the shell expansion velocity (e.g., Verhamme et al. 2006). Indeed, Rakic et al. (2011) found that for $z \approx 2.3$ LBGs, $V_{\rm offset}$ is about twice the blueshift of the interstellar absorption lines thought to arise in galactic winds. Hence, if the Lyα emission is back scattered off an outflowing medium, we expect $V_{\rm offset} \propto V_{\rm cir}$ which is consistent with our results. Alternatively, a static medium (or a medium without a clear bulk flow) with higher N(H I) for higher $V_{\rm cir}$ can also explain the correlation.

6 SUMMARY & CONCLUSIONS

Determining accurate redshifts for LAEs is challenging owing to the resonant scattering of Lyα photons with neutral hydrogen present in the ISM and in the CGM. Here we use CGM absorption lines, detected in the spectra of 8 background quasars, of 96 LAEs at $z \approx 3.3$ to calibrate the Lyα redshifts statistically. These LAEs are detected in 8 MUSE fields centered on the 8 bright quasars with redshifts 3.7–3.8. Our method for calibrating Lyα redshifts, which was pioneered by Rakic et al. (2011), relies on the assumption that the average (stacked) CGM absorption profiles of LAEs must be centered on the systemic velocity. This simply follows from the fact that the LAEs are randomly oriented with respect to the background quasars. Therefore, the CGM absorption, originating in outflows/accretion/co-rotating gas-disks, should have no preferred line of sight velocities. We measured $V_{\rm offset} = 169 \pm 10$ km s^{-1} and 178 ± 10 km s^{-1}, from the median and mean stacked absorption profiles, respectively. The $V_{\rm offset}$ obtained for the MUSE-detected LAEs in our sample is smaller than that measured for LBGs in the literature, likely due to the lower masses of LAEs compared to LBGs. $V_{\rm offset}$ shows positive trends with FWHM and a negative trend with EW$_0$. Finally, a sub-linear relation is obtained between $V_{\rm offset}$ and SFR, which, in turn, suggests that $V_{\rm offset}$ scales as the halo circular velocity.

Stacked CGM absorption profiles, as we obtained here, are a powerful tool to calibrate Lyα redshifts in a statistical manner, which can be applied to samples without systemic redshifts. Nevertheless, obtaining rest-frame optical nebular line diagnostics using future VLT/KMOS, Keck/MOSFIRE, and/or JWST/NIRSpec observations would be extremely useful to determine the systemic redshifts on a galaxy-by-galaxy basis, and to understand the physical properties of these high-z, presumably low-mass galaxies.

Acknowledgements: This study is based on observations collected at the European Organisation for Astronomical Research in the Southern Hemisphere under ESO programme(s): 094.A-0131(B), 095.A-0200(A), 096.A-0222(A), 097.A-0089(A), and 099.A-0159(A). SM acknowledges support from the Alexander von Humboldt Foundation, Germany. SC gratefully acknowledges support from Swiss National Science Foundation grant PP00P2_163824. JB acknowledges support by FCT/MCTES through national funds by grant UID/FIS/04434/2019 and through Investigador FCT Contract No. IF/01654/2014/CP1215/CT0003. AC and JR acknowledge support from the ERC starting grant 336736-CALENDS. MA acknowledges support from European Union's Horizon 2020 research and innovation programme under Marie Sklodowska-Curie grant agreement No 721463 to the SUNDIAL ITN, and from the Spanish Ministry of Economy and Competitiveness (MINECO) under grant number AYA2016-76219-P. FL and AV acknowledge support from the ERC starting grant ERC-757258-TRIPLE.

REFERENCES

Aguirre A., Schaye J., Theuns T., 2002, ApJ, 576, 1
Bacon R., et al., 2010, in Ground-based and Airborne Instrumentation for Astronomy III. p. 773508, doi:10.1117/12.856027
Behroozi P., Wechsler R. H., Hearin A. P., Conroy C., 2019, MNRAS, p. 1134
Bouwens R. J., et al., 2014, ApJ, 793, 115
Cantalupo S., Porciani C., Lilly S. J., Miniati F., 2005, ApJ, 628, 61
Cantalupo S., et al., 2019, MNRAS, 483, 5188
Cappellari M., et al., 2013, MNRAS, 432, 1862
Cassata P., et al., 2011, A&A, 525, A143
Chabrier G., 2003, PASP, 115, 763
Claeyssens A., et al., 2019, MNRAS, p. 2141
Cowie L. L., Songaila A., 1998, Nature, 394, 44
Díaz C. G., Ryan-Weber E. V., Cooke J., Koyama Y., Ouchi M., 2015, MNRAS, 448, 1240
Dijkstra M., Haiman Z., Spaans M., 2006, ApJ, 649, 14
Erb D. K., et al., 2014, ApJ, 795, 33
Fitzpatrick E. L., 1999, PASP, 111, 63
Gawiser E., et al., 2007, ApJ, 671, 278
Gronke M., 2017, A&A, 608, A139
Gronwall C., et al., 2007, ApJ, 667, 79
Hagen A., et al., 2016, ApJ, 817, 79
Hao C.-N., Huang J.-S., Xia X., Zheng X., Jiang C., Li C., 2018, ApJ, 864, 145
Hashimoto T., Ouchi M., Shimasaku K., Ono Y., Nakajima K., Rauch M., Lee J., Okamura S., 2013, ApJ, 775, 140
Hashimoto T., et al., 2015, ApJ, 812, 157
Hayes M., 2015, PASA, 32, e027
Heckman T. M., Alexandroff R. M., Borthakur S., Overzier R., Leitherer C., 2015, ApJ, 809, 147
Inami H., et al., 2017, A&A, 608, A2
Kennicutt Jr. R. C., 1998, ARA&A, 36, 189
Khostovan A. A., et al., 2018, arXiv e-prints,
Laursen P., Razoumov A. O., Sommer-Larsen J., 2009, ApJ, 696, 853
Leclercq F., et al., 2017, A&A, 608, A8
Madau P., Dickinson M., 2014, ARA&A, 52, 415
Malhotra S., Rhoads J. E., 2002, ApJ, 565, L71
Marino R. A., et al., 2018, ApJ, 859, 53
Maseda M. V., et al., 2017, A&A, 608, A4
Meurer G. R., Heckman T. M., Calzetti D., 1999, ApJ, 521, 64
Moster B. P., Naab T., White S. D. M., 2013, MNRAS, 428, 3121
Murphy M. T., Kacprzak G. G., Savorgnan G. A. D., Carswell R. F., 2019, MNRAS, 482, 3458
Murray N., Quataert E., Thompson T. A., 2005, ApJ, 618, 569

Muzahid S., Srianand R., Arav N., Savage B. D., Narayanan A., 2013, MNRAS, 431, 2885
Neufeld D. A., 1990, ApJ, 350, 216
O'Meara J. M., et al., 2015, AJ, 150, 111
Rakic O., Schaye J., Steidel C. C., Rudie G. C., 2011, MNRAS, 414, 3265
Rakic O., Schaye J., Steidel C. C., Booth C. M., Dalla Vecchia C., Rudie G. C., 2013, MNRAS, 433, 3103
Rauch M., et al., 2008, ApJ, 681, 856
Rauch M., Becker G. D., Haehnelt M. G., 2016, MNRAS, 455, 3991
Schaye J., Aguirre A., Kim T.-S., Theuns T., Rauch M., Sargent W. L. W., 2003, ApJ, 596, 768
Schlafly E. F., Finkbeiner D. P., 2011, ApJ, 737, 103
Shibuya T., et al., 2014, ApJ, 788, 74
Shibuya T., et al., 2018, PASJ, 70, S14
Sobral D., Santos S., Matthee J., Paulino-Afonso A., Ribeiro B., Calhau J., Khostovan A. A., 2018, MNRAS, 476, 4725
Steidel C. C., Erb D. K., Shapley A. E., Pettini M., Reddy N., Bogosavljević M., Rudie G. C., Rakic O., 2010, ApJ, 717, 289
Steidel C. C., et al., 2014, ApJ, 795, 165
Trainor R. F., Steidel C. C., Strom A. L., Rudie G. C., 2015, ApJ, 809, 89
Turner M. L., Schaye J., Steidel C. C., Rudie G. C., Strom A. L., 2014, MNRAS, 445, 794
Urrutia T., et al., 2019, A&A, 624, A141
Verhamme A., Schaerer D., Maselli A., 2006, A&A, 460, 397
Verhamme A., et al., 2018, MNRAS, 478, L60
Weilbacher P. M., Streicher O., Urrutia T., Jarno A., Pécontal-Rousset A., Bacon R., Böhm P., 2012, in Software and Cyberinfrastructure for Astronomy II. p. 84510B, doi:10.1117/12.925114
Wisotzki L., et al., 2016, A&A, 587, A98
Zahedy F. S., Rauch M., Chen H.-W., Carswell R. F., Stalder B., Stark A. A., 2019, arXiv e-prints,
Zheng Z., Miralda-Escudé J., 2002, ApJ, 568, L71

This paper has been typeset from a TEX/LATEX file prepared by the author.